Dalton Transactions

ROYAL SOCIETY OF CHEMISTRY

PAPER

View Article Online
View Journal | View Issue



Cite this: *Dalton Trans.*, 2024, **53**, 10655

# Loading and thermal behaviour of ZIF-8 metal–organic framework-inorganic glass composites†

Ashleigh M. Chester,[a] Celia Castillo-Blas,[a] Roman Sajzew,[b] Bruno P. Rodrigues,[b,c] Giulio I. Lampronti,[a,d] Adam F. Sapnik,[a] Georgina P. Robertson,[a,e] Matjaž Mazaj,[f] Daniel J. M. Irving,[e] Lothar Wondraczek,[b] David A. Keen[g] and Thomas D. Bennett*[a]

Received 26th March 2024,
Accepted 31st May 2024

DOI: 10.1039/d4dt00894d

rsc.li/dalton

Here we describe the synthesis of a compositional series of metal–organic framework crystalline-inorganic glass composites (MOF-CIGCs) containing ZIF-8 and an inorganic phosphate glass, $20Na_2O$–$10NaCl$–$70P_2O_5$, to expand the library of host matrices for metal–organic frameworks. By careful selection of the inorganic glass component, a relatively high loading of ZIF-8 (70 wt%) was achieved, which is the active component of the composite. A Zn···O–P interfacial bond, previously identified in similar composites/hybrid blends, was suggested by analysis of the total scattering pair distribution function data. Additionally, $CO_2$ and $N_2$ sorption and variable-temperature PXRD experiments were performed to assess the composites' properties.



## Introduction

Metal–organic frameworks (MOFs) are a class of three-dimensional hybrid materials comprising metal ions/clusters known as secondary building units (SBUs) and multidentate organic linkers, which assemble into porous architectures.[1–3] Due to the versatility offered by tailoring their structures, MOFs have been studied in applications such as photocatalysis,[4,5] sensing[5] and gas storage.[6]

A subset of the MOF family, zeolitic imidazolate frameworks (ZIFs), consists of metal ions (*e.g.* $Zn^{2+}$, $Co^{2+}$) tetrahedrally-coordinated to imidazolate-based linkers ($Im^-$), with a metal–Im–metal bridging angle similar to the Si–O–Si angle in zeolites.[2,7] The most well-studied ZIF is ZIF-8, $[Zn(mIm)_2]$, where mIm = 2-methylimidazolate, ($C_4H_5N_2^-$), which is commercially available as Basolite® Z1200. ZIF-8 has potential application in gas capture and separation, catalysis, drug delivery and sensing (Fig. 1a).[8,9]

However, MOFs, including ZIF-8, are typically synthesised as microcrystalline powders which are difficult to process and mould into macroscale, mechanically robust morphologies.[9,10] This, in addition to the relatively high economic cost of the precursor materials,[2] has limited their widespread application. To overcome these barriers, researchers have investigated composite materials using a MOF as the active component.[11] Examples of composite approaches include mixed-matrix membranes (MMMs) with organic polymers,[12] MOF–metal nanoparticle composites,[13,14] MOF-silica composites[15] and MOF-carbon composites.[16]

More recently, composites incorporating MOFs and glasses (hybrid or inorganic) have been proposed.[9,17] Glasses, also described as frozen liquids, are amorphous and display a

[a]*Department of Materials Science and Metallurgy, University of Cambridge, Cambridge, CB3 0FS, UK. E-mail: tdb35@cam.ac.uk*
[b]*Otto Schott Institute of Materials Research, University of Jena, Fraunhoferstrasse 6, 07743 Jena, Germany*
[c]*Fraunhofer Institute for Applied Optics and Precision Engineering, Albert-Einstein-Str. 7, 07745 Jena, Germany*
[d]*Department of Earth Sciences, University of Cambridge, Cambridgeshire, CB2 3EQ, UK*
[e]*Diamond Light Source Ltd., Diamond House, Harwell Campus, Didcot, Oxfordshire OX11 0DE, UK*
[f]*National Institute of Chemistry, Hajdrihova 19, 1000 Ljubljana, Slovenia*
[g]*ISIS Facility, Rutherford Appleton Laboratory, Harwell Campus, Didcot, Oxfordshire OX11 0QX, UK*

†Electronic supplementary information (ESI) available. See DOI: https://doi.org/10.1039/d4dt00894d

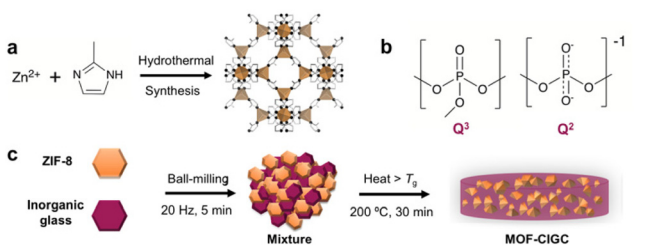


**Fig. 1** (a) Hydrothermal synthesis to produce ZIF-8, (b) Structural units present in sodium ultraphosphate glasses and (c) Schematic depicting the synthesis of MOF-CIGCs.

characteristic transition from a solid to a viscoelastic phase over a specific temperature range, characterised by a glass transition temperature ($T_g$).

In one example, a stimuli-responsive MOF, MIL-53(Al) [Al(OH)($O_2C$-$C_6H_4$-$CO_2$)], was combined with ZIF-62 glass ($a_g$ZIF-62), [Zn$(Im)_{1.75}(bIm)_{0.25}$] where Im = imidazolate $C_3H_3N_2^-$ and bIm = benzimidazolate $C_7H_5N_2^-$. The glass matrix stabilised the phase of MIL-53 with larger pores, leading to a composite with enhanced $CO_2$ uptake capacity.[18] Elsewhere, a composite comprising a porous coordination polymer (CP), [$Cu_2$(pzdc)$_2$(pyz)] where pzdc = 2,3-pyrazinedicarboxylate and pyz = pyrazine, and a glassy, non-porous CP, {[Cu(bib)$_{2.5}$]·2NT$f_2$}, where bib and NT$f_2$ are 1,4-bisimidazole butane and bis(trifluoromethylsulfonyl) amide respectively, was synthesised. The composite demonstrated enhanced selectivity when exposed to a gas mixture containing $N_2O$, $CO_2$ and $C_2H_4$.[19] Other examples include combining ZIF-8 and $a_g$ZIF-62 with fluoroaluminophosphate glasses[9,17] and sodium phosphate glasses.[20,21]

Here, this approach is extended by combining ZIF-8 and an ultraphopshate glass, 20$Na_2O$–10NaCl–70$P_2O_5$ (inorganic or 'IG') to create a compositional series of hybrid materials, namely metal–organic framework crystal inorganic glass composites (MOF-CIGCs).[22] The ultraphosphate glass consists of tetrahedral $PO_4$ units linked *via* bridging oxygen atoms,[23,24] which can be described as $Q^3$ and $Q^2$ units (Fig. 1b); $Q^3$ groups contain a P═O bond and three bridging oxygen atoms, while $Q^2$ groups have two bridging oxygen atoms. When sodium oxide and sodium chloride are added, the glass network is disrupted, and the sodium cations create ionic cross-links between the phosphate units.[25] The $Cl^-$ ions occupy the spaces between the phosphate chains without changing the short-range order of the glass.[26]

The characteristic non-bridging oxygen atom (P═O) in the tetrahedra of ultraphosphate glasses, where the [O]/[P] ratio is between 2.5 and 3, leads to their lower $T_g$ values when compared to similar silicate and germanate glasses. The 20$Na_2O$–10NaCl–70$P_2O_5$ glass in particular was selected for its low $T_g$ (168 °C), enabling a lower working temperature to prevent decomposition of the ZIF-8 during composite formation.

Previously, composites of ZIF-8 and a sodium phosphate glass, 50$Na_2O$-50$P_2O_5$ ($T_g$ = 300 °C) were successfully synthesised, with ZIF-8 loadings of 10–30 weight percent (wt%).[20] Here, we aim to extend this approach by increasing the number of available host matrices for crystalline MOFs, which remains scarce, and aim to obtain higher ZIF-8 loadings, which are imperative for utilisation of the composites in applications such as gas sorption and separation.

The composites were prepared *via* ball milling of the starting materials before pelletisation and heating above $T_g$, in line with previous methodologies (Fig. 1c).[17,18]

Initially, a compositional series was prepared with four different ZIF-8 loadings between 10–40 wt% to assess the MOF-CIGCs' properties. Care was taken in selecting the reaction conditions to prevent amorphisation and reduction of ZIF-8 crystallinity, which has been reported previously.[27,28] The resulting composites are named (ZIF-8)$_x$(Inorganic)$_{1-x}$ and the ball-milled physical mixtures prior to pelletisation and heat treatment are referred to as (ZIF-8)(Inorganic)(X/Y), consistent with prior nomenclature.[18] The thermal and chemical properties of these composites were investigated. Additionally, composites with higher ZIF-8 loadings (50, 60, 70 wt%) were synthesised to assess the maximum ZIF-8 loading by $CO_2$ and $N_2$ sorption experiments. Identifying the maximum MOF loading in composites is crucial for assessing trends in physical properties across a given compositional series and again, are important for their potential industrial implementation to identify the composition at which the composite performs the best.[29] In addition, the thermal behaviour of ZIF-8 in a MOF-CIGC with a 50 wt% ZIF-8 and 50 wt% inorganic glass was studied.

## Experimental

### Materials

($Zn(OAc)_2·2H_2O$, ≥98%) and 2-methylimidazole (99%) were purchased from Sigma Aldrich. Methanol (99.8%) was obtained from Fisher Scientific LTD and dimethyl sulfoxide (DMSO-$d^6$) (99.8 atom% D, containing 0.03% (v/v) tetramethylsilane (TMS)) was purchased from VWR International. All materials were used as received.

### ZIF-8 synthesis

The ZIF-8 synthetic procedure was modified from a previously reported methodology.[30] Zinc acetate dihydrate (0.3 g, 1.367 mmol) was added to 5 mL of deionised water. Separately, 2-methylimidazole (1.12 g, 14.495 mmol) was added to 5 mL of deionised water and sonicated to disperse the particles. The zinc acetate dihydrate solution was then poured over the linker solution and left to stand at room temperature for 24 hours. White nanocrystals were collected by centrifugation at 4000 rpm for five minutes and washed three times with methanol. The resulting product was dried under dynamic vacuum overnight at 80 °C. CHN analysis ($ZnC_8H_{10}N_4$) calculated/found: C 42.22%/42.71%, H 4.43%/4.56%, N 24.62%/24.36%.

### 20$Na_2O$–10NaCl–70$P_2O_5$ synthesis

$(NH_4)_2HPO_4$, $Na_2CO_3$ and NaCl were weighed and mixed in the desired proportions. The 50 g batches were then melted at 900 °C for an hour in alumina crucibles and quenched to form homogeneous glassy samples. After quenching, each glass was annealed at 210 °C. The annealing was performed in a furnace, where the glass was held isothermally for 30 minutes at 210 °C. Afterwards, the furnace was turned off and the glass was allowed to cool to room temperature inside the furnace, forming bulk pieces of glass. These pieces were then ground under an $N_2$ atmosphere to produce powdered glass samples.

### Composite synthesis

Powders of ZIF-8 and inorganic glass in various wt% ratios were added to a 10 mL stainless steel jar and shaken for five

 

minutes at 20 Hz with two five mm stainless steel grinding balls in a Retsch MM400 grinder mill. Approximately 130 mg was pelletised using three tonnes of force (0.22 GPa) for one minute before heating under vacuum to 200 °C for 30 minutes. The composites were then allowed to cool to room temperature under vacuum.

### Powder X-ray diffraction measurements (PXRD)

PXRD data were collected using a B3 Bruker D8 DAVINCI diffractometer equipped with a position sensitive LynxEye detector with Bragg–Brentano parafocusing geometry and Cu Kα radiation ($\lambda$ = 1.5418 Å) radiation was used through a 0.012 mm Ni filter. Samples were compacted into 5 mm disks on a low background silicon substrate and measured in 1–50° 2$\theta$ range. Pawley refinements were completed using TOPAS academic (V7) software.[31] Thompson-Cox-Hastings pseudo-Voigt (TCHZ) peak shapes and a simple axial divergence correction were used for the refinements. The lattice parameters were refined using the crystallographic information file of ZIF-8, in a 2$\theta$ range of 5–50°. The zero-point error was also refined.

### Thermogravimetric analysis (TGA)

TGA curves were recorded using a TA instruments Q-650 series differential scanning calorimeter. Approximately 5–10 mg of powdered samples were placed in open 90 μL alumina crucibles and heated at 10 °C min$^{-1}$ under argon. Heating cycles of 30–800 °C were used unless stated otherwise and all TGA data were analysed using TA Universal Analysis software.

### Differential scanning calorimetry (DSC)

DSC curves were performed using a NETSCH DSC 214 Polyma calorimeter. Approximately 5–10 mg of powdered samples were placed in sealed 70 μL aluminium crucibles with a pierced concave lid. Heating and cooling rates of 10 °C min$^{-1}$ under argon were used, with background corrections applied. Corrections were recorded prior to measurement using the same heating cycle on an empty aluminium crucible. An empty aluminium pan was used as a reference for all measurements and data were analysed using the Netzsch Proteus® software package.

### $^1$H Nuclear magnetic resonance (NMR) spectroscopy

Approximately 5–10 mg of each sample was dissolved in 35 wt% DCl/$D_2O$ (0.2 mL) and $d_6$-DMSO (1 mL) with TMS as a standard. Samples were run on Bruker Avance III HD 500 MHz at the Department of Chemistry, University of Cambridge. Data were analysed using Topsin version 4.1.1.[32]

### CHN microanalysis

CHN experiments were performed using approximately 5 mg of sample and were measured on a CE440 Elemental Analyser, EAI Exeter Analytical Inc. at the Department of Chemistry, University of Cambridge. Each sample was measured twice.

### Optical microscopy

A Leica MZ95 microscope and a Optika C-B10 CMOS with a resolution of 10 megapixels camera were used to obtain optical images of all samples.

### Scanning electron microscopy-X-ray energy dispersive spectroscopy (SEM-EDS)

SEM images were collected with a high-resolution FEI Nova Nano SEM 450 electroscope. Samples were mounted on a flat aluminium stub with conductive carbon tape and coated with gold. Information on imaging modes and accelerating voltages used for each sample can be found in the figure captions. An accelerating voltage of 15 kV was used for EDS analysis.

### Total X-ray scattering – pair distribution function (PDF)

Samples were ground and loaded into borosilicate capillaries with an inner diameter of 0.78 mm and a height of 3.9 cm before sealing. Total scattering data for PDF analysis were collected at the I15-1 beamline at the Diamond Light Source, UK (experiment reference EE20038, $\lambda$ = 0.189578 Å, 65.40 keV). Empty instrument (background) and empty capillary scans were run; all scans were collected in a $\sim 0.2 < Q < \sim 26$ Å$^{-1}$ range. The raw data were processed using GudrunX[33–35] in a $0.35 < Q < 20$ Å$^{-1}$ range and were corrected for background, container, multiple and Compton scattering. Fourier transformation of the processed total scattering data yielded real space pair distribution function, $G(r)$. Here, we use the $D(r)$ form to accentuate high $r$ correlations.

### Fourier transform infrared spectroscopy (FTIR)

FTIR spectra were collected on a Bruker Tensor 27 FTIR spectrometer in attenuated total reflectance (ATR) mode between 550 and 4000 cm$^{-1}$. Several milligrams of powder were placed directly on a diamond sample plate. A background was subtracted from all spectra prior to each measurement.

### Raman spectroscopy

Raman investigation was performed on a confocal Raman microscope (Renishaw InVia) equipped with a suitable edge-filter for the elastically scattered intensities and a 50× LD objective lens using 785 nm laser excitation to reduce fluorescence. Prior to sample characterisation, the grating and detector were calibrated against a single crystal silicon reference sample. Spectra were collected in the range of 100–1250 cm$^{-1}$ with ~1.2 cm$^{-1}$ resolution. Each measurement consisted of up to 60 individual accumulations at ~1 s accumulation time to maximise the signal-to-noise ratio without oversaturation of the detector.

### Gas adsorption

For the 10–40 wt% ZIF-8 composites and starting materials, $CO_2$ uptake capacities were recorded using a Micromeritics ASAP 2020 surface area and porosity analyser. Between 100 mg and 130 mg were degassed by heating under vacuum at 110 °C for two hours prior to measurement. $CO_2$ uptake isotherms

were measured using $CO_2$ at 273 K, with final $CO_2$ uptake values determined using Micromeritics MicroActive software. For the 50–70 wt% ZIF-8 composites, $CO_2$ uptake values were recorded at 273 and 283 K using an Autosorb iQ gas adsorption analyzer (Anton Paar) equipped with a temperature-controlled bath under the same activation conditions used for the 10–40 wt% ZIF-8 composites. For $N_2$ sorption experiments, an iQ3 gas adsorption analyzer (Anton Paar) was used at 77 K.

### Helium pycnometery/density

A Micromeritics Accupyc 1340 helium pycnometer was used to measure the density of the starting materials, using at least 120 mg of sample on a cycle of 10 measurements.

### Variable-temperature PXRD (VT-PXRD)

Samples were mixed with approximately 10 wt% by volume of Si standard powder using a mortar and pestle prior to measurement. Data were collected using a Bruker D8 Advance equipped with an MRI high-temperature chamber and a Vantec detector, using Cu Kα radiation ($\lambda$ = 1.5418 Å) under vacuum ($8.5 \times 10^{-3}$ mbar). Before measurement, height adjustments were performed to optimise the full width at half-maximum (FWHM) of the (111) silicon standard reflection at $2\theta$ ~28.45°. The samples were heated from 30 °C in 25 °C increments until 355 °C. Data were recorded in a $2\theta$ range of 6–36° in 0.04° steps and a time/step of 0.6 s.

Reported thermal expansion data for Si provided an accurate calculation of unit cell parameters for the Si standard. Peak positions could then be corrected for sample displacement. XRD data were refined sequentially using the reported crystallographic information file of ZIF-8, with atomic positions included but constrained. A broad Gaussian peak was added and refined sequentially to account for the diffuse scattering background of the inorganic glass. Subsequent refinements in the series were performed using the final values for the previous pattern as initial values. A Pearson VII function and an eighth-order Chebychev polynomial background were used to model the peak shape and the background respectively. Scale factors and unit cell parameters were refined individually for all scans. Data were analysed with TOPAS academic (V7) software.[31]

## Results and discussion

### Integrity of the ZIF-8 component

The ZIF-8 starting material was characterised by PXRD, Pawley refinement, SEM, TGA, CHN microanalysis and $^1$H NMR spectroscopy (Fig. S1–5†). The inorganic glass starting material was characterised by PXRD, SEM-EDS, TGA and DSC (Fig. S6–9†). The composites were synthesised according to the schematic in Fig. 1c. After pelletisation and heat treatment, compact and non-pulverulent pellets were produced (Fig. S10†). The integrity of the ZIF-8 component, integral for potential applications of the MOF-CIGCs, was determined using PXRD, FTIR, Raman and $^1$H NMR spectroscopy (Fig. S11–25†). The PXRD patterns of all composites comprise ZIF-8 Bragg peaks and diffuse scattering background from the inorganic glass, where the ZIF-8 peak height increases as the wt% ZIF-8 increases. However, only two Bragg peaks are visible in the $(ZIF\text{-}8)_{0.1}(Inorganic)_{0.9}$ composite (Fig. 2).

Pawley refinements of the PXRD patterns confirm that no extra peaks are present corresponding to recrystallisation of the glass or decomposition of either component (Fig. S12–15†), except for the $(ZIF\text{-}8)_{0.3}(Inorganic)_{0.7}$ composite in which an additional peak was observed which did not correspond to either material and is ascribed to minor recrystallisation of the glass.

Pawley refinements were also carried out on the PXRD patterns measured from the physical mixtures, the pelletised physical mixtures prior to heat treatment and the composites formed after heat treatment. The PXRD of the (ZIF-8)(Inorganic) (10/90) physical mixture contained ZIF-8 Bragg peaks, with a decrease in their height after pelletisation (Fig. S11†). After the thermal treatment at 200 °C for 30 minutes, Bragg peak intensities drastically decrease. A similar trend is observed for the other samples, where pelletisation culminates in decreased Bragg peak heights, with further decreases observed post heating. This decreased peak height is an indication of reduced crystallinity of ZIF-8, where a combination of ball milling, pelletisation and heat treatment, combined with the low wt% of ZIF-8 in the $(ZIF\text{-}8)_{0.1}(Inorganic)_{0.9}$ composite, obscured the visibility of the ZIF-8 Bragg peaks. Negligible changes in lattice parameter relative to pristine ZIF-8 are observed for the physical mixtures, pelletised mixtures and composite for all compositions (Tables S3–6†).

FTIR analysis shows that ZIF-8 is preserved for the higher wt% ZIF-8 composites (30–40 wt%), with only minor band broadening from the presence of the inorganic glass (Fig. S17†). The $(ZIF\text{-}8)_{0.2}(Inorganic)_{0.8}$ composite exhibits ZIF-8 bands, with considerable broadening consistent with the disordered structure of the glass. The $(ZIF\text{-}8)_{0.1}(Inorganic)_{0.9}$ and glass FTIR spectra are very similar, with only several ZIF-8

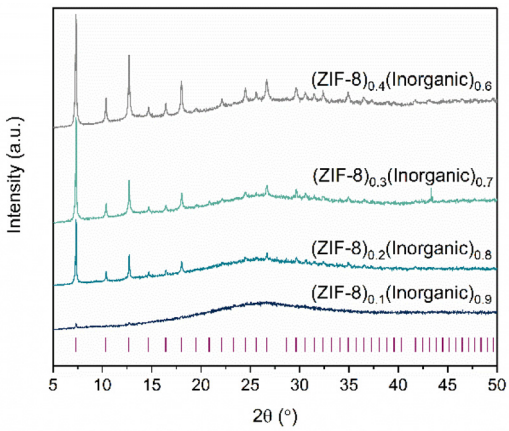


Fig. 2 PXRD patterns of the four composites (10–40 wt% ZIF-8), showing ZIF-8 Bragg peaks in all compositions except for the $(ZIF\text{-}8)_{0.1}(Inorganic)_{0.9}$ composite. An extra peak is visible at $2\theta$ = 43° for the $(ZIF\text{-}8)_{0.3}(Inorganic)_{0.7}$ composite.

bands present because of the higher content of inorganic glass and band broadening likely obscuring ZIF-8 bands. The FTIR analysis of the physical mixtures and composites show negligible changes after heat treatment for all compositions (Fig. S18†). This indicates preservation of the ZIF-8 and inorganic glass structures after composite synthesis. Additionally, the Raman spectra of the composites display bands corresponding to the ZIF-8 framework, with broadening evident on account of the inorganic glass, a similar effect shown in the FTIR data (Fig. S19†).

Acid-digested $^1$H NMR was used to further assess the ZIF-8 structure in the composites. It has been used previously to determine the preservation of ZIF materials post heat treatment by assessing the integration of the linker peaks.[9,17] For the $(ZIF\text{-}8)_{0.1}(Inorganic)_{0.9}$ composite (Fig. 20–21), only one proton environment is visible in the $^1$H NMR spectrum. However, both proton environments of the 2-methylimidazole linker are present in the $^1$H NMR spectra of the 20–40 wt% ZIF-8 composites (Fig. S22–25†), with the correct integrated peak ratios, indicating no decomposition of the linker during the composite preparation.

The low wt% of ZIF-8 in the $(ZIF\text{-}8)_{0.1}(Inorganic)_{0.9}$ composite led to difficulties in assessing ZIF-8's preservation after composite formation. However, the presence of two ZIF-8 peaks in the PXRD, as well as ZIF-8 bands present in the Raman spectrum, suggests its integrity was maintained post composite synthesis.

### Microscopy and thermal analysis

SEM images of the $(ZIF\text{-}8)_{0.3}(Inorganic)_{0.7}$ composite show ZIF-8 particles embedded within the glass matrix surface (Fig. 3a) and evidence of inorganic glass flow around the ZIF-8 particles within the bulk (Fig. 3b). By observing the inside of the 10–40 wt% ZIF-8 composites, it is evident that the glass fully surrounds the ZIF-8 particles (Fig. S26†). This includes the $(ZIF\text{-}8)_{0.1}(Inorganic)_{0.9}$ composite, which shows the presence of ZIF-8 particles after composite formation. SEM-EDS on the composites shows a heterogenous elemental distribution in the samples, indicating separate domains of ZIF-8 and inorganic glass (Fig. S27–30†).

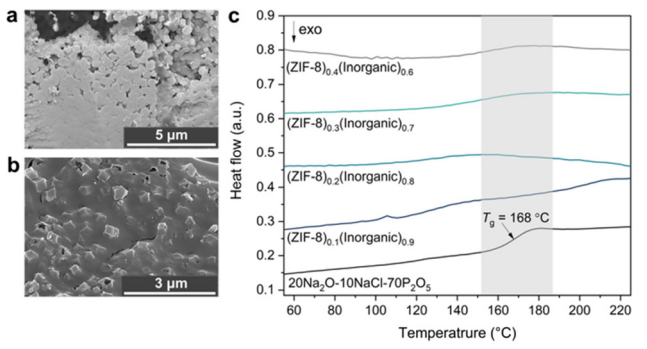


**Fig. 3** SEM images of the $(ZIF\text{-}8)_{0.3}(Inorganic)_{0.7}$ composite on (a) Surface of the pellet, (b) Bulk within the pellet and (c) Second DSC upscan of all four composites and the inorganic glass.

Mass loss features in TGA of the physical mixtures indicate a lower onset of decomposition compared to the starting materials, with $T_d$s in the range of 318–355 °C for the 10, 20, 30 and 40 wt% ZIF-8 physical mixtures (Fig. S31–34†), lower than the $T_d$s of both starting materials (ZIF-8 $T_d$ = 607 °C and inorganic glass $T_d$ = 660 °C). This lower onset of decomposition may be the result of interactions between the two components, which has been reported elsewhere.[9] This lower onset of decomposition is also observed for the composite samples, with $T_d$s in the range of 301–364 °C (Fig. S35a and S36–39†). For comparison, TGA measurements were also performed on ZIF-8 controls under the reaction conditions (Fig. S35b†), which also demonstrate decreased $T_d$s relative to ZIF-8. This decreased in $T_d$ is evident after ball milling, which has been reported previously.[36] No significant changes in $T_d$ occur after pelletisation and heat treatment. However, the decreased $T_d$ is smaller than the reduction in $T_d$ observed for the composites, suggesting possible interfacial interaction.

DSC was used to identify the inorganic glass' $T_g$ to confirm the integrity of the inorganic glass structure after composite synthesis. The second and third DSC upscans from all composites except the $(ZIF\text{-}8)_{0.1}(Inorganic)_{0.9}$ composite show noticeable endothermic features in the temperature range around the $T_g$ of the inorganic glass indicated by the shaded region in Fig. 3c. No other features were observed in the DSC upscans from these samples, except for distinct endothermic peaks in the first upscans corresponding to surface water loss from the inherently hygroscopic phosphate glass (Fig. S40–44†).

The $(ZIF\text{-}8)_{0.1}(Inorganic)_{0.9}$ composite has two, unassigned features in the second and third upscans close to the temperature range of the inorganic glass' transition temperature (Fig. S40†).

### Pair distribution function analysis

Pair distribution function (PDF) analysis gives atom-atom correlation histograms[37,38] and is increasingly used to analyse the local structure of materials.[39] The positions of the peaks in the PDF correspond to atom-atom correlation distances within a given material. The intensity of these peaks is determined by the scattering power of the specific atom pairs within the material, as well as the frequency with which the distance between atom pairs is observed.[39,40] Synchrotron X-ray total scattering measurements were collected on the I15-1 beamline at the Diamond Light Source (Methods) and the data were normalised to produce total scattering structure factors, $S(Q)$, of the four composites and starting materials (Fig. S45–46†). The $S(Q)$ of ZIF-8 and the composites contain ZIF-8 Bragg peaks observed in the PXRD data. The inorganic glass $S(Q)$ shows an absence of Bragg features, as expected. These structure factors were Fourier transformed to produce the real-space PDFs ($D(r)$).

The PDF of ZIF-8 contains the main correlations (Fig. 4, peaks and distances labelled A-E) of the 2-methylimidazolate ring joined to Zn and the Zn–Zn correlation F, consistent with the crystallographic structure of ZIF-8 (Fig. S47†). Key correlations in the inorganic glass PDF have been assigned (Fig. S48†) based on a crystalline phase of sodium phosphates

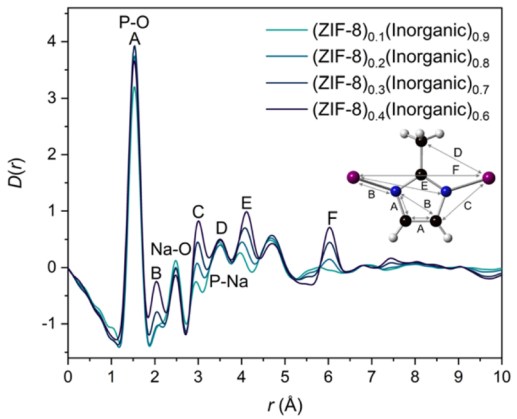


**Fig. 4** X-ray pair distribution functions, $D(r)$s, of all four composites with the assigned correlations from the parent materials, namely A–F from the 2-methylimidazolate ring – Zn structure of ZIF-8 and inorganic peak assignments at 1.54 Å, 2.48 Å and 3.45 Å for P–O, Na–O and P–Na respectively. Zinc (pink), carbon (black), nitrogen (blue) and hydrogen (white) atoms are displayed in the inset.

($Na_3P_3O_9$) and previous total scattering experiments.[23,24,41] The PDFs of the 20–40 wt% ZIF-8 composites contain correlations from both ZIF-8 and the inorganic glass, with several correlations, such as A (ZIF-8) and the P–O bond (inorganic glass) overlapping (Fig. 4). Correlations corresponding to ZIF-8 increase with increased ZIF-8 incorporation, whereas the peaks from the inorganic glass $D(r)$s decrease. The increased intensity of such correlations is more evident in the ZIF-8 peaks, concordant with the larger relative changes in ZIF-8 proportions across the compositional series. ZIF-8 correlations are difficult to discern in the PDF of the $(ZIF\text{-}8)_{0.1}(Inorganic)_{0.9}$ composite, where its PDF resembles the inorganic glass' PDF closely.

Interfacial interactions between the ZIF-8 and inorganic glass could not be readily deduced from the $D(r)$s alone. To understand these interactions, multiple linear regression (MLR) was performed on the composite $D(r)$s. Previously, this MLR approach was used to obtain possible interactions between ZIFs (glassy and crystalline) and sodium phosphate glasses, in which potential interface peaks were suggested at $r$ ~3.2–3.3 Å. The same methodology was applied here; each composite $D(r)$ was fitted according to Eqn 1 for $0 < r < 10$ Å, where $C_1$ and $C_2$ are linked to the amount of inorganic glass and ZIF-8 in the composite respectively (Fig. S49†). This $r$-range was selected because of the observed differences in Bragg peak shapes for pristine ZIF-8 and a ZIF-8 control sample that had undergone the same reaction conditions of the composites (Fig. S5†); the broadened ZIF-8 Bragg peaks in the composites reduce the PDF peak intensities at higher-$r$ relative to those from the pristine ZIF-8 and fitting data to higher-$r$ would skew regression results.

$$\text{Composite } D(r) = C_1(IG\ D(r)) + C_2\ (\text{ZIF-8}\ D(r)) \quad (1)$$

Good agreement was obtained for the composite $D(r)$s with 20–40 wt% ZIF-8 using the starting material $D(r)$s. The residuals from these fits contain two key peaks, the first peak at $r$ ~1.35 Å can be assigned to the C–C/C–N bond in the 2-methylimidazolate ring of ZIF-8. The second peak at $r$ ~3.2 Å is not present in either starting material PDF, nor is it present in the empty capillary $D(r)$ used for data processing. Moreover, this peak is consistent with previous results on similar composites and is in the region of bond lengths involving O, P and Zn atoms obtained from several crystalline zinc phosphate phases (Fig. S50†). As a tentative conclusion, this second peak could correspond to a potential interaction between the phases in which Zn and P atoms are bridged *via* an oxygen atom, the same interaction identified previously in ZIF-8/$50Na_2O$-$50P_2O_5$ [20] and $a_g$ZIF-62/$30Na_2O$-$70P_2O_5$ systems.[21]

However, the residual obtained from the fitting of the $(ZIF\text{-}8)_{0.1}(Inorganic)_{0.9}$ composite shows a negative peak at $r$ ~1.6 Å, consistent with the Si–O bond length in the borosilicate capillary (Fig. S51†) and suggests that the empty capillary data have been over-subtracted during data normalisation. The presence of a positive or negative PDF peak at this $r$-value indicates a potential lack of efficient capillary subtraction from the data. Here, the sample's peaks partially overlap the Si–O peak from the capillary which makes this challenging to observe in the PDF. However, it is detected in the linear regression differential. Hence, the capillary scattering used in the data normalisation for this sample was reduced by 7.5%; the new, adjusted $D(r)$ and $S(Q)$ were visually very similar to the original, unadjusted $D(r)$ and $S(Q)$ (Fig. S51†). MLR was then rerun on this re-normalised sample, producing a similar residual (peaks at $r$ ~1.35 Å and $r$ ~3.2 Å) but without the peak at $r$ ~1.6 Å. The proposed interface peak's position and intensity are largely unchanged, and the residual overall now resembles the 20–40 wt% ZIF-8 residuals more closely (Fig. 5).

### $CO_2$ uptake and stability

$CO_2$ gas sorption measurements were performed on a pelletised sample of ZIF-8 (0.22 GPa), because of the broadening and reduction in Bragg peak height after applying pressure,

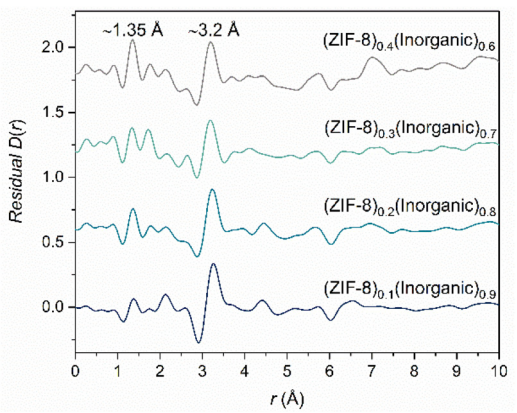


**Fig. 5** Residuals obtained from the MLR fitting of the four composite samples (10–40 wt% ZIF-8), using an adjusted $D(r)$ for the $(ZIF\text{-}8)_{0.1}(Inorganic)_{0.9}$ composite to counteract capillary subtraction issues (see main text for details).

giving a better comparison *versus* pristine ZIF-8, where pressure has been linked to gas uptake and separation ability of ZIF-8.[20,42,43] Previous work on MOF-CIGCs comprising ZIF-8 and a different phosphate glass, $50Na_2O$-$50P_2O_5$, show a small decrease in uptake capacity of pelletised (0.22 GPa) ZIF-8 *versus* pristine ZIF-8.[20] The maximum uptake values of the composites are in the range 0.16–0.66 mmol $g^{-1}$ (Table S9†) which, as expected, increases as the ZIF-8 loading increases (Fig. S52†). All composites have a higher uptake of $CO_2$ than the dense, non-porous inorganic glass which shows minimal uptake (0.056 mmol $g^{-1}$). These results confirm that porosity, an intrinsic property of MOFs, has been retained within the MOF-CIGCs.

The air stability of the $(ZIF\text{-}8)_{0.4}(Inorganic)_{0.6}$ composite was tested to determine whether ZIF-8 reduced the known hygroscopic nature of ultraphosphate glasses.[21,44] The inorganic glass and $(ZIF\text{-}8)_{0.4}(Inorganic)_{0.6}$ were left in air for three weeks. After this time, the inorganic glass displayed a visible wetting effect (Fig. S53a†) caused by its water uptake, though PXRD shows that it maintained an amorphous structure. The composite retains its non-pulverulent, compact nature, but water uptake is also evident in the wetting of the composite's surface after air exposure (Fig. S53b†). PXRD analysis of the $(ZIF\text{-}8)_{0.4}(Inorganic)_{0.6}$ after air exposure indicates a decrease in height of the Bragg peaks of the composite over time, suggesting that the ZIF-8 structure is maintained in the composite even after three weeks air exposure, although some reduction in crystallinity occurs (Fig. S54b†).

This water uptake is also evident in the first DSC upscans of both samples. DSC results from the glass after three weeks air exposure display a large endotherm in the first upscan at 105.7 °C showing that a large amount of water had been taken up by the glass (Fig. S54–56†). The first upscan shows the inorganic glass' $T_g$ at the same temperature as the pristine glass, however the second and third upscans indicate two $T_g$ features, one near the expected inorganic glass' $T_g$ (168 °C) and another much lower at 65 °C. This decrease in $T_g$ is a well-studied effect in ultraphosphate glasses which have been exposed to water vapour. Water is able to depolymerise the glass network, decreasing the extent of cross-linking and in turn, decreasing the $T_g$.[23]

The first DSC upscan of the composite has a large endothermic feature at 89.1 °C corresponding to surface water loss, confirming the hygroscopic nature of the composite. The inorganic $T_g$ is present in this upscan before the onset of decomposition. However, the second DSC upscan shows a shifted $T_g$ to a temperature of 137.3 °C, a decrease in the original $T_g$ of about 30 °C. This corresponds to depolymerising of the glass network as described above, but the decrease is less than the inorganic glass control, suggesting that ZIF-8 might stabilise the glass structure to some extent.

### Maximum ZIF-8 incorporation

To determine the maximum loading of ZIF-8 in the glass matrix, samples where the ZIF-8 proportion was increased to 50, 60 and 70 wt%, were synthesised. Non-powdery, cohesive pellets were produced for the 50–70 wt% ZIF-8 composites (Fig. S57†) and PXRD analysis, including Pawley refinement, confirms the presence of ZIF-8 in the composites (Fig. S58-59†). However, the heights of the ZIF-8 Bragg peaks decrease above 50 wt% ZIF-8, despite the increased loading of ZIF-8, which is opposite to what is observed for the 10–40 wt% ZIF-8 composites. Examination of the ZIF-8 Bragg peaks of the physical mixtures, pelletised mixtures and corresponding composites for the 50–70 wt% ZIF-8 samples show a decrease in peak height post pelletisation, accompanied by peak broadening. The peak height partially recovers after heating (Fig. S59†), as observed in the ZIF-8 controls (Fig. S5†). This partial recovery is not observed for the 10–40 wt% ZIF-8 composites. A possible explanation for the differences observed for the 50–70 wt% ZIF-8 samples relative to the 10–40 wt% ones is that the glass matrix can shield the ZIF-8 from structural changes during pelletisation, but is unable to do so when the content of inorganic glass in the composite is too low (<*ca.* 50%), where it cannot add resistance against structural changes/collapse of the ZIF-8. This effect has been observed in similar composites with ZIF-8.[9,20]

$N_2$ at 77 K and $CO_2$ adsorption experiments at 273 K and 283 K were performed on the 50–70 wt% ZIF-8 composites (Fig.S60a–c†) to determine the optimum ZIF-8 loading for gas sorption efficiency as a supplement to the $CO_2$ measurements on the 10–40 wt% ZIF-8 composites (Fig. S52†). For the 50–70 wt% ZIF-8 composites specifically, $CO_2$ sorption experiments at 273 and 283 K indicate the optimum loading for ZIF-8 in the glass is 50 wt% (Fig. S60a–c†). After 50 wt% ZIF-8 loading, the sorption capacity for $CO_2$ decreases. This is consistent with the PXRD results, where a decrease in Bragg peak heights are observed after 50 wt% ZIF-8 loading.

Analysis of the $CO_2$ uptake capacity across the whole compositional series shows that the maximum $CO_2$ uptake at a relative pressure of 0.025 increases non-linearly as the wt% ZIF-8 increases in the composite, until a maximum point at 50 wt% ZIF-8 (Fig. 6). Anomalous points are observed at 20 wt% and 50 wt% ZIF-8, where the uptake values are higher than expected from the trend. The jump at 20 wt% can be partially explained by observing the PXRD differences in the physical mixture, pelletised mixture and composite of the 20 wt% ZIF-8 samples (Fig. S11†), where minimal loss in peak height is observed after ball milling, pelletisation and heat treatment. This is in contrast to the composites with 10, 30 and 40 wt% ZIF-8, which show decreases in peak height after pelletisation and heat treatment. The differences in peak height can arise from varying ratios of inorganic glass and ZIF-8, which can affect the composite's microstructure, including cracks and microscale voids between the heterogenous domains observed in the SEM images of the composites (Fig. S26–30†), which in turn could affect the diffusion of $CO_2$ molecules through the composite. This effect on $CO_2$ sorption has been observed in composites comprising ZIF-8 and $50Na_2O$-$50P_2O_5$.[20]

Additionally, a relatively large increase in $CO_2$ uptake can be observed between 40 wt% and 50 wt% ZIF-8. The isotherms for 10–40 wt% ZIF-8 composites show hysteresis, with iso-

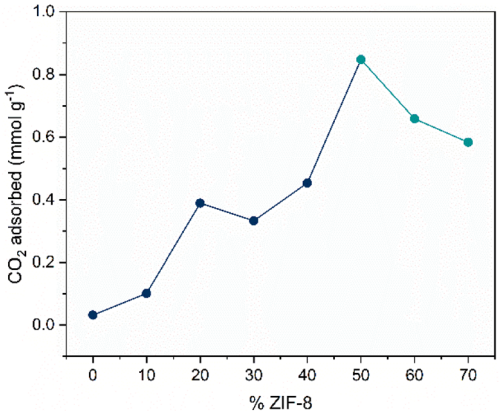


**Fig. 6** $CO_2$ uptake *versus* wt% ZIF-8 incorporated in the 10–70 wt% composites at a relative pressure of 0.025. Different coloured circles are used for 50–70 wt% samples because of the different equipment used, see Experimental methods.

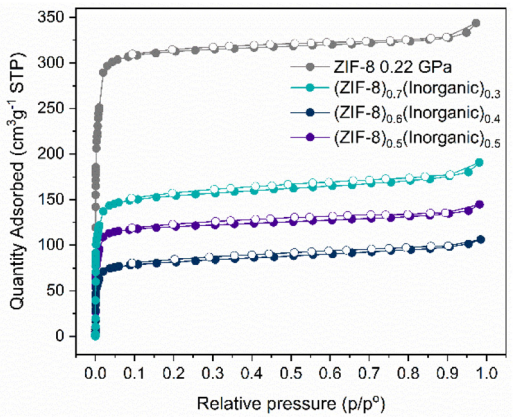


**Fig. 7** $N_2$ gas sorption isotherms at 77 K for pelletised ZIF-8 (0.22 GPa), $(ZIF\text{-}8)_{0.5}(Inorganic)_{0.5}$, $(ZIF\text{-}8)_{0.6}(Inorganic)_{0.4}$ and $(ZIF\text{-}8)_{0.7}(Inorganic)_{0.3}$ composites. Closed and open circles indicate adsorption and desorption respectively.

therm shapes deviating from pelletised ZIF-8 (Fig. S52†). However, the shape of the 50–70 wt% ZIF-8 composites' isotherms exhibit pelletised ZIF-8 more closely, with minimal hysteresis which can help explain the jump after 40 wt%. Overall, a clear, qualitative increase in $CO_2$ uptake is observed as the wt% ZIF-8 increases, up to a maximum point of 50 wt% ZIF-8.

$N_2$ adsorption experiments were not performed on the inorganic glass as it is dense and non-porous and would result in minimal uptake of $N_2$, similar to what is observed for its $CO_2$ uptake. This would preclude BET surface area analysis on the glass. However, $N_2$ sorption experiments were performed on pristine ZIF-8 and pelletised ZIF-8 (0.22 GPa) (Fig. S60d and Table S11†). BET analysis on pristine ZIF-8 indicates a surface area of 1867 $m^2\ g^{-1}$, which is reduced to 1318 $m^2\ g^{-1}$ after pelletisation. Both samples exhibit a Type I isotherm consistent with that reported for ZIF-8, indicating microporosity of the samples.[45] The reduction in BET surface area is consistent with the decreased $CO_2$ uptake observed for pelletised ZIF-8 *versus* pristine ZIF-8 and the reduced peak height in the PXRDs (Fig. S5†).

$N_2$ adsorption experiments indicate retained porosity of ZIF-8 in the 50–70 wt% ZIF-8 composites, with reasonable BET surface areas (327–628 $m^2\ g^{-1}$) calculated for the composites (Fig. 7 and Table S11†).

$N_2$ capacity is highest for the $(ZIF\text{-}8)_{0.7}(Inorganic)_{0.3}$ and lowest for $(ZIF\text{-}8)_{0.6}(Inorganic)_{0.4}$, a different trend to what is observed for the $CO_2$ uptake. Discrepancies in uptake trends can be attributed to differences in the polarisability and kinetic diameters of $CO_2$ and $N_2$ adsorbates. The composites' $CO_2$ isotherms (Fig. S60†) exhibit a near-linear shape until a relative pressure of *ca.* 0.03, commonly observed for this type of ZIF and observed for the ZIF-8 and pelletised ZIF-8 samples.[45] As the wt% ZIF-8 increases in the 50–70 wt% ZIF-8 composites, there is a slight deviation from linearity to a Langmuir-type isotherm at 273 K when compared to the isotherms at 283 K (Fig. S60†). This deviation suggests the presence of polar sorption sites promoting interactions with $CO_2$ at 283 K or the occurrence of additional voids in the samples facilitating faster diffusion. Additionally, higher uptake at 283 K in comparison to 273 K in the case of $(ZIF\text{-}8)_{0.7}(Inorganic)_{0.3}$ composite suggests either chemisorption *or* enhanced diffusion taking place at higher temperatures because of additional pore openings. The absence of visible desorption hysteresis for the $(ZIF\text{-}8)_{0.7}(Inorganic)_{0.3}$ isotherm at 283 K indicates that additional pore openings likely contribute to the differences in the isotherms, which explains the improved BET surface area for this composite. The $CO_2$ isotherms at 273 K and 283 K, as well as the $N_2$ isotherms, for the 50–70 wt% ZIF-8 composites show negligible desorption hysteresis, in contrast to the 10–40 wt% ZIF-8 composites, where visible hysteresis is observed. This could be the result of the inorganic glass partially encapsulating the ZIF-8 in the composites with higher wt% inorganic glass. However, when the inorganic content decreases, additional pore openings of the 50–70 wt% ZIF-8 composites lead to higher $CO_2$ uptake values and negligible hysteresis.

Overall, these results suggest suitability of the composites for applications involving $N_2$ uptake and separation, whereby the mechanical barriers of pristine ZIF-8 are circumvented.

### Thermal behaviour of ZIF-8 in the glass matrix

To assess the effect of the inorganic glass on the response of ZIF-8 to temperature, especially considering the degree of flexibility exhibited by ZIF-8 in response to external stimuli, *in situ* variable temperature PXRD (VT-PXRD) measurements were performed on the $(ZIF\text{-}8)_{0.5}(Inorganic)_{0.5}$ composite and a ZIF-8 control sample, both heated to 355 °C (Fig. S62–64†). The control was prepared under the reaction conditions of 0.22 GPa, 200 °C for 30 minutes. TGA on the $(ZIF\text{-}8)_{0.5}(Inorganic)_{0.5}$ composite shows a $T_d$ of 300 °C (Fig. S61†).

The behaviour of the $(ZIF\text{-}8)_{0.5}(Inorganic)_{0.5}$ composite upon heating between 30 and 130 °C shows a slight increase

in the cell volume of ZIF-8 in this temperature range (linear thermal expansion coefficient, $\alpha_a$ = 10.5 × $10^{-6}$ $K^{-1}$). This is consistent with molecular dynamics simulations, which predict positive thermal expansion of ZIF-8, in corroboration with experimental VT-FTIR data showing slight lattice expansion below 200 °C (Fig. S64†).[46] At 155 °C, as the inorganic glass enters its supercooled liquid state, there is small unit cell volume decrease of 0.31% until 180 °C.

After 180 °C, there is a linear increase of the unit cell until 300 °C ($\alpha_a$ = 22 × $10^{-6}$ $K^{-1}$). Positive thermal expansion in this region is consistent with pristine, evacuated ZIF-8 in the literature ($\alpha_a$ = 9.2 × $10^{-6}$ $K^{-1}$), but ZIF-8 in the composite has a larger coefficient of linear expansion (Fig. 8).[47] At 300 °C, the unit cell volume begins to decrease as sample decomposition occurs, also evident in the increased Rietveld $R_{wp}$ fitting values and a noticeable decrease in Bragg peak heights (Fig. S64 and Table S13†). Overall, the ZIF-8 encased within the glass matrix behaves in a similar manner to pristine ZIF-8 except across the glass transition temperature range.

The behaviour of ZIF-8 in this composite at $T_g$ is in contrast with composites consisting of flexible MIL-118, $[Al_2(OH)_2(C_{10}O_8H_2)]$, encased in $a_g$ZIF-62, where the unit cell volume increased as the glass matrix softened.[48] A possible, tentative explanation for this difference is that during composite formation the ZIF-8 is heated to a $T_w$ of 200 °C, where it expands and is held in this slightly expanded form by the inorganic glass because of interactions between the two phases; interactions have been suggested by PDF and thermal analysis. Moreover, several studies have investigated the behaviour and flexibility of the 2-methylimidazolate linker in ZIF-8 across various temperature ranges, including the temperatures used in this study, which would support the framework's ability to deform slightly.[49,50] As the composite is heated to the $T_g$ in the VT-PXRD experiments, this slightly expanded unit cell can revert to its thermodynamic equilibrium value as the viscosity of the glass starts to decrease and its thermal expansion coefficient increases. This behaviour is linked to the noticeable increase in thermal expansion coefficient of phosphate glasses at $T_g$.[51] After the glass transition range, the ZIF-8 expands faster ($\alpha_a$ = 22 × $10^{-6}$ $K^{-1}$) within the now less-viscous glass, exhibiting a larger lattice coefficient than pristine ZIF-8 in the literature ($\alpha_a$ = 9.21 × $10^{-6}$ $K^{-1}$) from 200–500 °C.[47]

These results shed light on the thermal behaviour of the composite, which is important for its potential use in applications requiring dynamic temperature control. It is also crucial from a microscale perspective, where the thermal response is closely linked to the MOF's pore size and shape, which is important for applications such as gas uptake/storage and separation. For these applications specifically, pore size affects host–guest interactions and lattice stiffening, observed for some MOFs such as ZIF-8 when heated. These effects can improve gas capture performance and selectivity.[52] Additionally, the results provide insight into the effect that ball milling, pressure and heating have on pristine ZIF-8 *versus* ZIF-8 encased in an inorganic glass matrix, shown by the contrasting changes in unit cell volume between the samples across the experimental heating range.

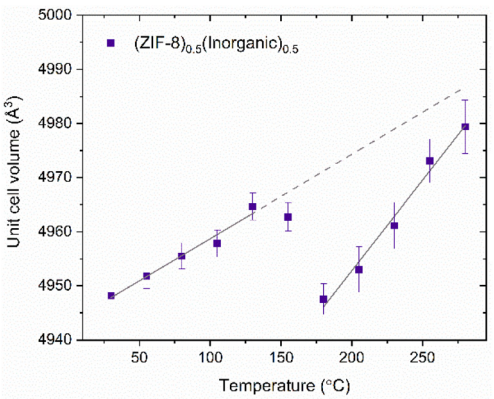


**Fig. 8** Refined unit cell volume of the $(ZIF\text{-}8)_{0.5}(Inorganic)_{0.5}$ composite, where two regions of volumetric expansion have been fitted. The straight-line fit of first region (30–130 °C) has been extrapolated (dotted line). The slopes of both lines were calculated using the linear thermal expansion coefficients obtained from the corresponding lattice parameter-temperature graph.

## Conclusions

In this study, we have described the fabrication of a compositional series of MOF-CIGCs, $(ZIF\text{-}8)_x(20Na_2O\text{-}10NaCl\text{-}70P_2O_5)_{1-x}$, expanding the library of potential host matrices for crystalline MOFs. Crystalline ZIF-8 (20–40 wt%) was successfully stabilised in an inorganic glass matrix, confirmed by $^1$H NMR, FTIR, Raman spectroscopy and PXRD analysis. Difficulties arose when assessing preservation of ZIF-8 within the $(ZIF\text{-}8)_{0.1}(Inorganic)_{0.9}$ composite because of the low wt% of ZIF-8 in the composite. Nonetheless, evidence for the presence of ZIF-8 in this composite was provided by Raman spectroscopy, PXRD (where two ZIF-8 Bragg peaks were evident), PDF MLR analysis and SEM. Additionally, $CO_2$ sorption analysis indicated an increased uptake of $CO_2$ by the $(ZIF\text{-}8)_{0.1}(Inorganic)_{0.9}$ composite relative to the inorganic glass, also suggesting preservation of ZIF-8 in the composite.

Distinct endothermic features in the temperature range around the inorganic glass' $T_g$ were visible in the DSC upscans of the 20–40 wt% ZIF-8 composites, indicating preservation of the inorganic component. The $(ZIF\text{-}8)_{0.1}(Inorganic)_{0.9}$ composite displayed two, unassigned features in the DSC upscans in the region of the inorganic glass' transition temperature.

SEM imaging revealed the flow of the glass around the ZIF-8 particles, showing reasonable chemical compatibility between ZIF-8 and the glass in the 10–40 wt% ZIF-8 composites.

Additionally, air stability tests on the $(ZIF\text{-}8)_{0.4}(Inorganic)_{0.6}$ composite indicated retention of ZIF-8's crystallinity, despite the decreased height of the ZIF-8 Bragg peaks, after three weeks of air exposure. Furthermore, the composite pellet maintained its cohesive morphology despite its water uptake.

Interfacial interactions, which are key for mechanical performance, between the ZIF-8 and glass matrix were analysed by total scattering PDF data on the 10–40 wt% ZIF-8 composites, in which a potential Zn···O–P bond was proposed based on the location of a residual peak obtained from MLR analysis, present in the residuals of all four composites.

The thermal behaviour of a MOF-CIGC containing 50 : 50 wt% ZIF-8: inorganic glass was studied by VT-PXRD. Rietveld refinements indicated a small unit cell contraction of the ZIF-8 in the composite over a temperature range coinciding with the inorganic glass' glass transition, allowing small changes in the ZIF-8's lattice parameter as the glass entered its supercooled liquid state, in line with the known decreased viscosity and increased thermal expansion of inorganic glasses upon heating to $T_g$. Such information is important for determining suitable applications of these composites, where thermal expansion may or may not be desired.

A relatively high ZIF-8 loading (70 wt%), the active component for applications, was achieved for the glass matrix. Importantly, the $CO_2$ adsorption capability of the MOF-CIGCs increased non-linearly as the incorporation of ZIF-8 increased up until 50 wt% ZIF-8, showing the gas uptake capability of ZIF-8 was retained in the synthesised composites. After 50 wt% ZIF-8, the $CO_2$ adsorption values decreased, in line with the decreased height of the ZIF-8 Bragg peaks of the composites. $N_2$ adsorption experiments were also performed on the composites comprising higher amounts of ZIF-8 (50–70 wt%), where the composites demonstrated adequate $N_2$ uptake. Gas sorption results indicate these composites would be desirable for applications requiring uptake capacity in devices consisting of different shapes, in which the microcrystalline nature of ZIF-8 and other MOFs is unsuitable.

## Author contributions

AMC, CCB, DAK, TDB and LW conceptualised the project. AMC wrote the manuscript with contributions from all authors. ZIF-8 and composite samples were synthesised by AMC, the inorganic glass was synthesised by BPR. AMC and CCB analysed the inorganic glass. FTIR, PXRD, Pawley refinements and thermal analysis were performed and analysed by AMC. $^1$H NMR was performed by technicans at the Department of Chemistry, University of Cambridge; AMC prepared the samples and analysed the results. $CO_2$ sorption experiments on the 10–40 wt% ZIF-8 composites were performed by AMC. $CO_2$ and $N_2$ sorption experiments on the 50–70 wt% ZIF-8 composites were carried out by MM. Raman analysis was performed by RS and LW. Total scattering PDF data was collected by AMC, CCB, GPR, DJMI, DAK and AFS. Subsequent data processing was completed by AMC, with DAK and CCB assisting with interfacial regression analysis. VT-PXRD data was collected and processed by GIL and Rietveld refinements were performed by GIL. DAK, TDB and LW supervised the project and acquired funding.

## Conflicts of interest

There are no conflicts to declare.

## Acknowledgements

A. M. C. and C. C. B. acknowledge Leverhulme Trust Research Project Grant (RPG-2020-005). LW acknowledges funding from the Carl Zeiss Foundation through its Breakthrough program (2019). T. D. B. thanks the Royal Society for both a University Research Fellowship (URF\R\211013) and a research grant (RGS\R2\212221). G. P. R. acknowledges funding from the UKRI and Diamond Light Source under studentship number STU0366. A. F. S. acknowledges the EPSRC under industrial CASE scheme along with Johnson Matthey PLC (JM11106). M. M. acknowledges financing from Slovenian Research Agency program (P1-0021). A. M. C. acknowledges technicians at the Department of Chemistry, University of Cambridge, for collecting $^1$H NMR and CHN microanalysis data. A. M. C. also acknowledges Luke Rochford for data collection of the VT-PXRD results.

## References

1 G. Maurin, C. Serre, A. Cooper and G. Férey, *Chem. Soc. Rev.*, 2017, **46**, 3104–3107.
2 B. Chen, Z. Yang, Y. Zhu and Y. Xia, *J. Mater. Chem. A*, 2014, **2**, 16811–16831.
3 H. Furukawa, K. E. Cordova, M. O'Keeffe and O. M. Yaghi, *Science*, 2013, **341**, 1230444.
4 Y. Chen, A.-G. Liu, P.-D. Liu, Z.-T. Chen, S.-Y. Liu and B. Li, *J. Mater. Chem. A*, 2023, **11**, 18236–18246.
5 S. Li, B. Wang, G. Liu, X. Li, C. Sun, Z. Zhang and X. Wang, *Inorg. Chem. Front.*, 2024, **11**, 1561–1572.
6 S. E. Henkelis, S. M. Vornholt, D. B. Cordes, A. M. Z. Slawin, P. S. Wheatley and R. E. Morris, *CrystEngComm*, 2019, **21**, 1857–1861.
7 Y.-Q. Tian, C.-X. Cai, X.-M. Ren, C.-Y. Duan, Y. Xu, S. Gao and X.-Z. You, *Chem. – Eur. J.*, 2003, **9**, 5673–5685.
8 C. Hao, D. Zhou, J. Xu, S. Hong, W. Wei, T. Zhao, H. Huang and W. Fang, *J. Mater. Sci.*, 2021, **56**, 9434–9444.
9 L. Longley, C. Calahoo, T. J. F. Southern, R. C. Evans, L. Wondraczek and T. D. Bennett, *Dalton Trans.*, 2021, **50**, 3529–3535.
10 J. Hou, A. F. Sapnik and T. D. Bennett, *Chem. Sci.*, 2020, **11**, 310–323.
11 Q.-L. Zhu and Q. Xu, *Chem. Soc. Rev.*, 2014, **43**, 5468–5512.
12 Y. Lu, H. Zhang, J. Y. Chan, R. Ou, H. Zhu, M. Forsyth, E. M. Marijanovic, C. M. Doherty, P. J. Marriott, M. M. B. Holl and H. Wang, *Angew. Chem., Int. Ed.*, 2019, **58**, 16928–16935.
13 J. Yu, C. Mu, B. Yan, X. Qin, C. Shen, H. Xue and H. Pang, *Mater. Horiz.*, 2017, **4**, 557–569.

14 Z.-S. Zhao, Y. Zhang, T. Fang, Z.-B. Han and F.-S. Liang, *ACS Appl. Nano Mater.*, 2020, **3**, 6316–6320.
15 K. Tanaka, T. Muraoka, D. Hirayama and A. Ohnish, *Chem. Commun.*, 2012, **48**, 8577.
16 L. N. McHugh, A. Terracina, P. S. Wheatley, G. Buscarino, M. W. Smith and R. E. Morris, *Angew. Chem., Int. Ed.*, 2019, **58**, 11747–11751.
17 L. Longley, C. Calahoo, R. Limbach, Y. Xia, J. M. Tuffnell, A. F. Sapnik, M. F. Thorne, D. S. Keeble, D. A. Keen, L. Wondraczek and T. D. Bennett, *Nat. Commun.*, 2020, **11**, 5800.
18 J. Hou, C. W. Ashling, S. M. Collins, A. Krajnc, C. Zhou, L. Longley, D. N. Johnstone, P. A. Chater, S. Li, M.-V. Coulet, P. L. Llewellyn, F.-X. Coudert, D. A. Keen, P. A. Midgley, G. Mali, V. Chen and T. D. Bennett, *Nat. Commun.*, 2019, **10**, 2580.
19 X. Zheng, M. Kato, Y. Uemura, D. Matsumura, I. Yagi, K. Takahashi, S. Noro and T. Nakamura, *Inorg. Chem.*, 2023, **62**, 1257–1263.
20 C. Castillo-Blas, A. M. Chester, R. P. Cosquer, A. F. Sapnik, L. Corti, R. Sajzew, B. Poletto-Rodrigues, G. P. Robertson, D. J. M. Irving, L. N. McHugh, L. Wondraczek, F. Blanc, D. A. Keen and T. D. Bennett, *J. Am. Chem. Soc.*, 2023, **145**, 22913–22924.
21 A. M. Chester, C. Castillo-Blas, R. Sajzew, B. P. Rodrigues, R. Mas-Balleste, A. Moya, J. E. Snelson, S. M. Collins, A. F. Sapnik, G. P. Robertson, D. J. M. Irving, L. Wondraczek, D. A. Keen and T. D. Bennett, *Chem. Sci.*, 2023, **14**, 11737–11748.
22 A. M. Chester, C. Castillo-Blas, L. Wondraczek, D. A. Keen and T. D. Bennett, *Chem. – Eur. J.*, 2022, **28**, e202200345.
23 R. K. Brow, *J. Non-Cryst. Solids*, 2000, **263–264**, 1–28.
24 U. Hoppe, R. Kranold, A. Barz, D. Stachel, J. Neuefeind and D. A. Keen, *J. Non-Cryst. Solids*, 2001, **293–295**, 158–168.
25 M. I. Ojovan and W. E. Lee, in *An Introduction to Nuclear Waste Immobilisation*, Elsevier, 2014, pp. 245–282.
26 B. P. Rodrigues, R. Limbach, G. Buzatto De Souza, H. Ebendorff-Heidepriem and L. Wondraczek, *Front. Mater.*, 2019, **6**, 128.
27 T. D. Bennett, P. J. Saines, D. A. Keen, J.-C. Tan and A. K. Cheetham, *Chem. – Eur. J.*, 2013, **19**, 7049–7055.
28 E. F. Baxter, T. D. Bennett, A. B. Cairns, N. J. Brownbill, A. L. Goodwin, D. A. Keen, P. A. Chater, F. Blanc and A. K. Cheetham, *Dalton Trans.*, 2016, **45**, 4258–4268.
29 C. W. Ashling, D. N. Johnstone, R. N. Widmer, J. Hou, S. M. Collins, A. F. Sapnik, A. M. Bumstead, P. A. Midgley, P. A. Chater, D. A. Keen and T. D. Bennett, *J. Am. Chem. Soc.*, 2019, **141**, 15641–15648.
30 L. Sheng, F. Yang, C. Wang, J. Yu, L. Zhang and Y. Pan, *Mater. Lett.*, 2017, **197**, 184–187.
31 A. A. Coelho, *J. Appl. Crystallogr.*, 2018, **51**, 210–218.
32 *Bruker, TopSpin, Version 4.0.7*, Bruker, Billerica, MA, 2019.
33 D. A. Keen, *J. Appl. Crystallogr.*, 2001, **34**, 172–177.
34 A. K. Soper, *GudrunN and GudrunX: programs for correcting raw neutron and X-ray diffraction data to differential scattering cross section*, 2011.
35 A. K. Soper and E. R. Barney, *J. Appl. Crystallogr.*, 2011, **44**, 714–726.
36 S. Cao, T. D. Bennett, D. A. Keen, A. L. Goodwin and A. K. Cheetham, *Chem. Commun.*, 2012, **48**, 7805.
37 K. W. Chapman, K. A. Beyer, H. Zhao and P. J. Chupas, *CrystEngComm*, 2013, **15**, 9377.
38 S. J. L. Billinge, *Philos. Trans. R. Soc., A*, 2019, **377**, 20180413.
39 I. Romero-Muñiz, A. Mavrandonakis, P. Albacete, A. Vega, V. Briois, F. Zamora and A. E. Platero-Prats, *Angew. Chem., Int. Ed.*, 2020, **59**, 13013–13020.
40 M. J. Cliffe, W. Wan, X. Zou, P. A. Chater, A. K. Kleppe, M. G. Tucker, H. Wilhelm, N. P. Funnell, F.-X. Coudert and A. L. Goodwin, *Nat. Commun.*, 2014, **5**, 4176.
41 J. M. Cole, X. Cheng and M. C. Payne, *Inorg. Chem.*, 2016, **55**, 10870–10880.
42 Q. Ma, H. Jin and Y. Li, *Chem. – Eur. J.*, 2020, **26**, 13137–13141.
43 Y. Hu, Z. Liu, J. Xu, Y. Huang and Y. Song, *J. Am. Chem. Soc.*, 2013, **135**, 9287–9290.
44 V. V. Brazhkin, J. Akola, Y. Katayama, S. Kohara, M. V. Kondrin, A. G. Lyapin, S. G. Lyapin, G. Tricot and O. F. Yagafarov, *J. Mater. Chem.*, 2011, **21**, 10442.
45 N. Missaoui, H. Kahri and U. B. Demirci, *J. Mater. Sci.*, 2022, **57**, 16245–16257.
46 B. Xu, Y. Mei, Z. Xiao, Z. Kang, R. Wang and D. Sun, *Phys. Chem. Chem. Phys.*, 2017, **19**, 27178–27183.
47 T. D. Bennett, PhD Thesis, University of Cambridge, 2012.
48 C. W. Ashling, G. I. Lampronti, T. J. F. Southern, R. C. Evans and T. D. Bennett, *Inorg. Chem.*, 2022, **61**, 18458–18465.
49 F.-X. Coudert, *ChemPhysChem*, 2017, **18**, 2732–2738.
50 T. Ueda, T. Yamatani and M. Okumura, *J. Phys. Chem. C*, 2019, **123**, 27542–27553.
51 P. Lunkenheimer, A. Loidl, B. Riechers, A. Zaccone and K. Samwer, *Nat. Phys.*, 2023, **19**, 694–699.
52 J. Hao, D. J. Babu, Q. Liu, P. A. Schouwink, M. Asgari, W. L. Queen and K. V. Agrawal, *Chem. Mater.*, 2021, **33**, 4035–4044.